

The aerostatic response and stability performance of a wind turbine tower-blade coupled system considering blade shutdown position

S.T. Ke^{*1,2}, L. Xu^{1a} and Y.J. Ge^{2b}

¹Department of Civil Engineering, Nanjing University of Aeronautics and Astronautics, 29 Yudao Road, Nanjing 210016, China

²State Key Laboratory for Disaster Reduction in Civil Engineering, Tongji University, 1239 Siping Road, Shanghai 200092, China

(Received May 25, 2017, Revised August 9, 2017, Accepted August 12, 2017)

Abstract. In the strong wind shutdown state, the blade position significantly affects the streaming behavior and stability performance of wind turbine towers. By selecting the 3M horizontal axis wind turbine independently developed by Nanjing University of Aeronautics and Astronautics as the research object, the CFD method was adopted to simulate the flow field of the tower-blade system at eight shutdown positions within a single rotation period of blades. The effectiveness of the simulation method was validated by comparing the simulation results with standard curves. In addition, the dynamic property, aerostatic response, buckling stability and ultimate bearing capacity of the wind turbine system at different shutdown positions were calculated by using the finite element method. On this basis, the influence regularity of blade shutdown position on the wind-induced response and stability performance of wind turbine systems was derived, with the most unfavorable working conditions of wind-induced buckling failure of this type of wind turbines concluded. The research results implied that within a rotation period of the wind turbine blade, when the blade completely overlaps the tower (Working condition 1), the aerodynamic performance of the system is the poorest while the aerostatic response is relatively small. Since the influence of the structure's geometrical nonlinearity on the system wind-induced response is small, the maximum displacement only has a discrepancy of 0.04. With the blade rotating clockwise, its wind-induced stability performance presents a variation tendency of first-increase-then-decrease. Under Working condition 3, the critical instability wind speed reaches its maximum value, while the critical instability wind speed under Working condition 6 is the smallest. At the same time, the coupling effect between tower and blade leads to a reverse effect which can significantly improve the ultimate bearing capacity of the system. With the reduction of the area of tower shielded by blades, this reverse effect becomes more obvious.

Keywords: wind turbine; numerical simulation; shutdown position; ultimate bearing capacity; wind-induced stability

*Corresponding author, Associate Professor, E-mail: keshitang@163.com

^a Postgraduate, E-mail: luxunuaa@163.com

^b Professor, E-mail: yaojunge@tongji.edu.cn

1. Introduction

The wind turbine tower-blade system is a typical wind-sensitive structure, especially when the wind turbine stays in the shutdown state under high-speed wind. Investigations on the overall stability performance of wind turbines have significant engineering and theoretical values (Arani and Mohamed 2015, Germanischer Lloyd 2010, Han 2017). In current design specifications (GB/T 20319-2006) and research results (Hemmatpour *et al.* 2016, Shaltout 2015, Mawer and Kalumba 2016), the influence of blade position in the shutdown state has barely been considered. Different blade shutdown positions significantly affect the aerodynamic and stability performances of the whole wind turbine tower-blade coupled system.

To analyze the wind resistance of wind turbine towers at different blade shutdown positions, scholars (Ke *et al.* 2016, Ke *et al.* 2016, Duquette and Visser 2003, Tempel 2006, Ke *et al.* 2016) conducted a series of studies based on large-eddy simulation and finite element method. They discussed the influences of blade shielding area within a single rotation period on the dynamic property, wind-induced response, tower streaming and wake flow features, as well as the influence regularity of shielding effect difference caused by different blade shutdown positions on the surface wind pressure and overall rise/drag coefficients. Focusing on the stability performance study of wind turbine tower-blade systems, Madsen *et al.* (2013), Zhao *et al.* (2010) studied the tower buckling behavior caused by tower, cabin load and tower gravity, by selecting a large-scale wind turbine with bottom door as the research object. Jeong *et al.* (2013), Li *et al.* (2017) analyzed the aeroelastic stability of composite blades used in large-scale wind turbines and predicted the possibility and related positions of blade local buckling. Available studies mainly concentrated on the aerodynamic performance, tower streaming and wake flow features, and wind-induced response of wind turbine systems at different blade shutdown positions, as well as analyses of single-factor (tower or blade) wind-induced stability. However, few studies have conducted qualitative or quantitative analyses on the influences of shutdown position on the buckling stability and ultimate bearing capacity of overall wind turbine structures.

Hence, by selecting the 3M horizontal axis wind turbine independently developed by Nanjing University of Aeronautics and Astronautics as the research object, the CFD method was adopted to simulate the flow field of the wind turbine tower-blade system at eight shutdown positions in a single rotation period of blades. The effectiveness of the simulation method was validated by comparing the simulation results with standard curves. In addition, the dynamic property, aerostatic response, buckling stability and ultimate bearing capacity of the wind turbine system at different shutdown positions were calculated by using the finite element method. On this basis, the influence regularity of blade shutdown position on the wind-induced response and stability performance of wind turbine systems was derived, with the most unfavorable working conditions of wind-induced buckling failure of this type of wind turbines concluded. The research results of this study are of important reference values for the refined anti-wind design of large-scale wind turbines.

2. Project overview

The wind turbine system investigated in this study has a height of 85 m, a tower-top radius of 2 m, and a tower bottom radius of 2.5 m. The tower is a full thickness-varying structure, with a top wall thickness of 30 mm and a bottom wall thickness of 60 mm. The cut-in wind speed of wind

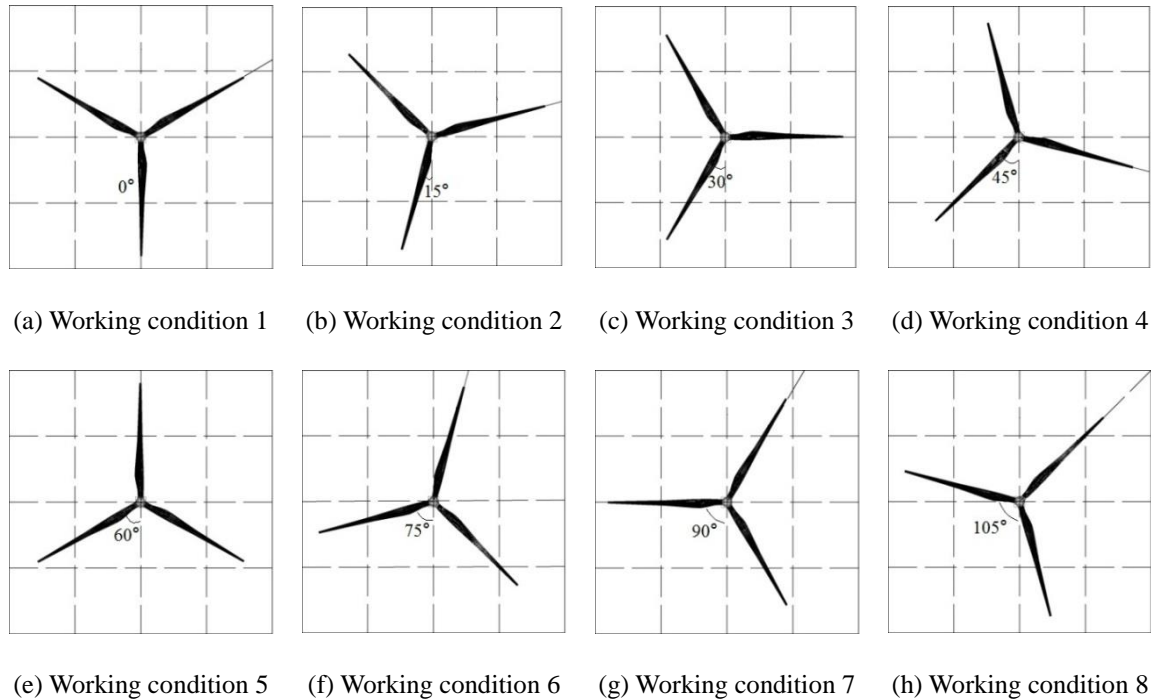


Fig. 1 Illustration of calculating working condition at different blade shutdown positions.

wheel is 3.5 m/s, the rated wind speed is 12.5 m/s, and the cut-out wind speed is 25 m/s. The tilt angle of the wind wheel is 5° . The rotation speed of wind wheel ranges between 9 and 19 rpm, while the drift speed is $0.5^\circ/\text{s}$. An angle of 120° exists between two adjacent blades, which uniformly distribute along the circumferential direction. The blade length is 44.5 m. The length, width, and height of the cabin are 12 m, 4 m and 4 m, respectively.

According to the relative position between blade and tower, the moment when the blade completely overlaps the tower is defined as Working condition 1, by considering the periodicity existing during the rotation of a three-blade system. During the blades rotating clockwise, each 15° accounts for one working condition, thus, there are eight working conditions. In addition, the blade which completely overlaps the tower in Working condition 1 is labeled as Blade 1, and the rest two along the clockwise direction are labeled as Blade 2 and Blade 3, respectively. The single-period blade rotation direction under different working conditions is shown in Fig. 1.

3. Rationale and algorithm of tower-blade coupling

Due to the larger blade quality and scavenging area, the results obtained taking into account the effect of blade on the tower is closer to the actual situation. In order to obtain the coupled vibration equation of the tower and the blade, this paper uses the generalized coordinate method to establish the dynamic equation of the wind power generation system. The five degrees of freedom are the displacement of the tower in the direction of the wind speed y_t , the swing angle of the blade θ_b , the

rotation angle of the rotor θ_r , the rotation angle of the generator spindle θ_g and the rotation angle of yaw θ_w . Since large wind turbines mostly use the way of active yaw, the yaw rotation can be considered as uniform speed when the motor drives the yaw system. As is followed in the Figs. 2 and 3, the four degrees of freedom after removing the rotation angle of yaw are used to describe the wind power generation system. At the same time the dynamic model of the wind power generation system can be expressed in the next equation

$$M\ddot{q} + C\dot{q} + Kq = Q(q, \dot{q}, t, u) \quad (1)$$

Where, M , C and K are the mass matrix, damping matrix and stiffness matrix of the system; Q is the generalized force of the system ($Q = [NF_T \quad NF_T r_b \quad T_r \quad T_g]$); N is the number of blades for wind turbines; F_T is a concentrated force when the wind is exerted to the blade length of r_b ; $NF_T r_b$ is a concentrated moment when the wind is exerted to the blade length of r_b ; T_r and T_g are rotor torque and generator spindle torque, respectively; Q is the generalized coordinate of the system ($q = [y_t \quad \theta_h \quad \theta_r \quad \theta_g]$).

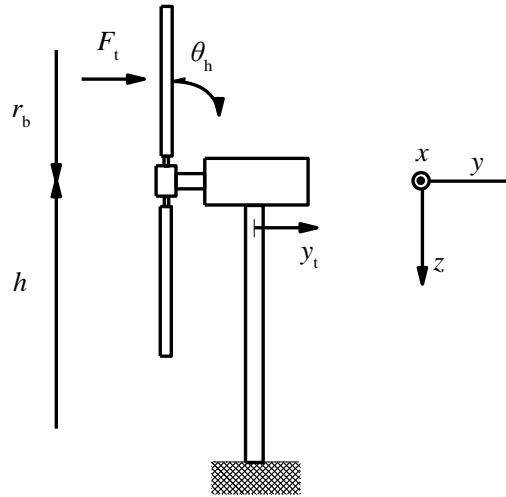


Fig. 2 Schematic diagram of the wind turbine blade and tower

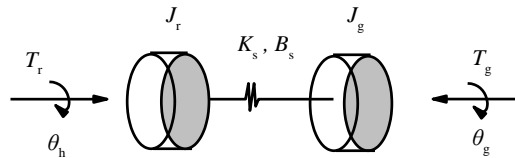


Fig. 3 Schematic diagram of the wind turbine drive system

Lagrange equation

$$\frac{d}{dt} \left(\frac{\partial E_k}{\partial \dot{q}_i} \right) - \frac{\partial E_k}{\partial q_i} + \frac{\partial E_d}{\partial \dot{q}_i} + \frac{\partial E_p}{\partial q_i} = Q_i \quad (2)$$

Where, E_k , E_d and E_p are the kinetic energy, the energy consumption and the potential energy of the system; q_i is the generalized coordinates for the degree of freedom of the i ; Q_i is the generalized force for the degree of freedom of the i .

E_k , E_d and E_p are respectively expressed as

$$E_k = \frac{m_t}{2} \dot{y}_t^2 + \frac{N}{2} m_b (\dot{y}_t + r_b \dot{\theta}_h)^2 + \frac{J_r}{2} \dot{\theta}_r^2 + \frac{J_g}{2} \dot{\theta}_g^2 \quad (3)$$

$$E_d = \frac{B_t}{2} \dot{y}_t^2 + \frac{N}{2} B_b (r_b \dot{\theta}_h)^2 + \frac{B_s}{2} (\dot{\theta}_r - \dot{\theta}_g)^2 \quad (4)$$

$$E_p = \frac{K_t}{2} y_t^2 + \frac{N}{2} K_b (r_b \theta_h)^2 + \frac{K_s}{2} (\theta_r - \theta_g)^2 \quad (5)$$

Where, m_t is the quality of tower and the engine room; J_r is the rotational inertia of the rotor; J_g is the moment of inertia of the generator; B_t , B_b and B_s is the damping of the tower, blade and transmission system; K_t , K_b and K_s is the stiffness of the tower, blade and transmission system.

Put q , Q , E_k , E_d and E_p into Lagrange equation and simplifying

$$(Nm_b + m_t) \ddot{y}_t + Nm_b r_b \ddot{\theta}_h + B_t \dot{y}_t + K_t y_t = NF_T \quad (6)$$

$$Nm_b r_b^2 \ddot{\theta}_h + Nm_b r_b^2 \ddot{y}_t + NB_b r_b^2 \dot{\theta}_h + NK_b r_b^2 \theta_h = NF_T r_b \quad (7)$$

$$J_r \ddot{\theta}_r + B_s \dot{\theta}_r - B_s \dot{\theta}_g + K_s \theta_r - K_s \theta_g = T_r \quad (8)$$

$$J_g \ddot{\theta}_g - B_s \dot{\theta}_r + B_s \dot{\theta}_g - K_s \theta_r + K_s \theta_g = -T_g \quad (9)$$

When expressed in matrix form, the mass matrix M , the damping matrix C and the stiffness matrix K are shown as follows

$$M = \begin{bmatrix} Nm_b + m_t & Nm_b r_b & 0 & 0 \\ Nm_b r_b & Nm_b r_b^2 & 0 & 0 \\ 0 & 0 & J_r & 0 \\ 0 & 0 & 0 & J_g \end{bmatrix} \quad (10)$$

$$C = \begin{bmatrix} B_t & 0 & 0 & 0 \\ 0 & NB_b r_b^2 & 0 & 0 \\ 0 & 0 & B_s & -B_s \\ 0 & 0 & -B_s & B_s \end{bmatrix} \quad (11)$$

$$K = \begin{bmatrix} K_t & 0 & 0 & 0 \\ 0 & NK_b r_b^2 & 0 & 0 \\ 0 & 0 & K_s & -K_s \\ 0 & 0 & -K_s & K_s \end{bmatrix} \quad (12)$$

The concentrated force (F_T), rotor torque (F_T), Generator torque (F_T) producing when the wind is exerted to the blade length of r_b can be obtained by the next equation

$$F_T = \frac{\rho \pi R^2}{2} C_T v^2 \quad (13)$$

$$T_r = \frac{\rho \pi R^3}{2} C_Q v^2 \quad (14)$$

$$T_g = \frac{T_r}{n} \eta \quad (15)$$

Where, ρ is the density of air; R is the blade radius; C_T is the thrust coefficient; v is a combination of wind speed; C_Q is the torque coefficient; n is the transmission ratio of gearbox; η is the transmission efficiency.

4. CFD numerical simulation

4.1 Calculation domain and mesh generation

To ensure that the flow can fully develop, the calculation domain is set as 12D×5D×5D (flow direction X × spanwise direction Y × vertical direction Z, D is the wind wheel diameter). The wind turbine locates at 3D of the calculation domain inlet. Since the blade surface warps complicatedly, the hybrid grid discrete form is adopted. The whole calculation domain is divided into two parts: the inner region and the external region. The inner region is meshed with tetrahedral meshes, with the local meshes around the wind turbine refined. In the external region, high-quality hexahedral meshes are used. The total amount of meshes is 1 2400 000. The calculation domain and detailed mesh generation are shown in Fig. 4.

Table 1 Grid quality and windward pressure coefficient under different grid schemes

	Total number of grids	Grid quality	Maximum skew	windward pressure coefficient
Scheme 1	105	0.11	0.96	1.10
Scheme 2	560	0.35	0.85	0.96
Scheme 3	830	0.51	0.80	0.85
Scheme 4	1240	0.61	0.73	0.80
Scheme 5	3000	0.63	0.71	0.78

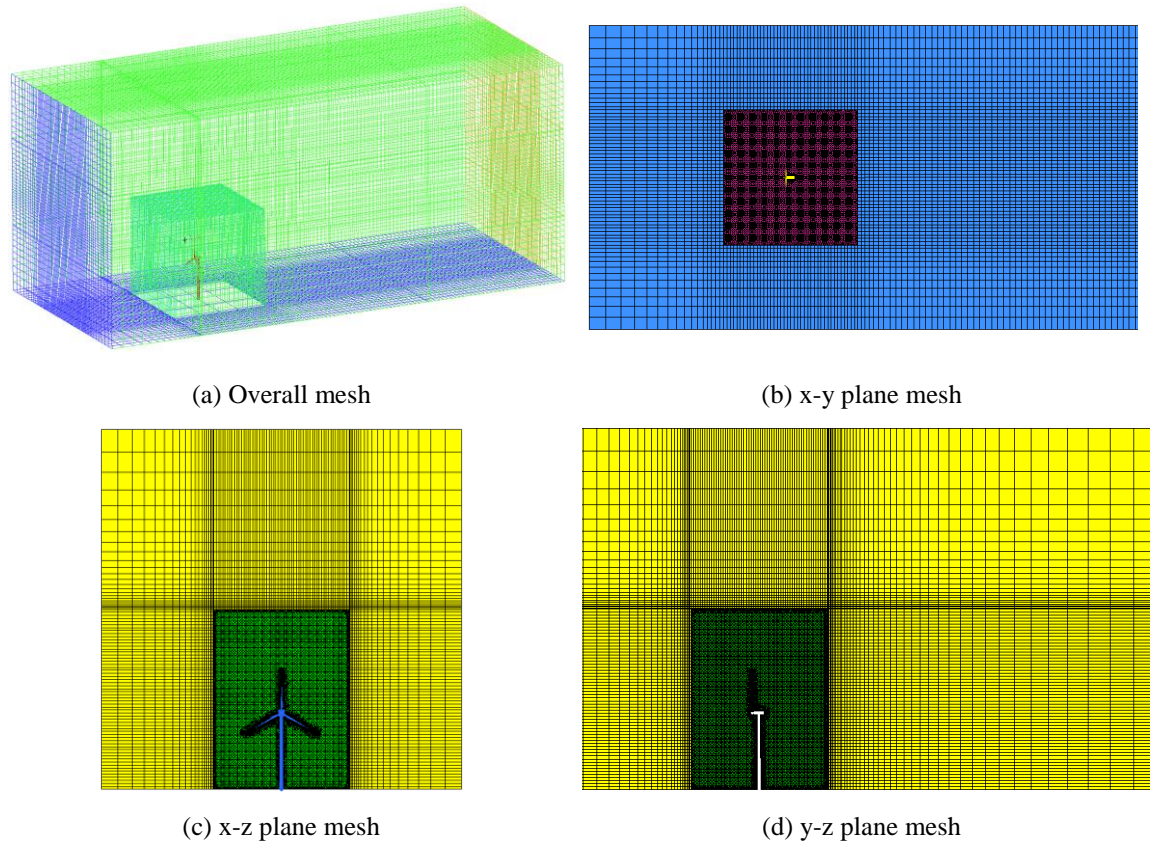


Fig. 4 Calculation domain and mesh generation

Table 1 lists the grid quality and the windward pressure coefficient under different grid schemes. It is found that the grid quality increases with the increase of the total number of grids, and the maximum skew of the grid and the pressure coefficient of the windward side gradually decrease. There is no significant difference in the grid quality and calculation results between the number of 12 million 400 thousand grids and the number of 30 million grids. The scheme four was adopted balancing calculation precision and efficiency. Please refer to the revised draft for details.

4.2 Model selection and inflow boundary setting

4.2.1 Model selection

In this paper, the 3D calculation steady implicit algorithm is set as the calculation method. The standard k- ϵ model is set as the turbulence model (Laan *et al.* 2015). The coupling between velocity component and pressure in the momentum equation is settled by using the SIMPLEC algorithm (Skrzypiński and Gaunaa 2015). During calculation, the turbulent kinetic energy, turbulent dissipation term, and the momentum equation are all discretized by using the second order upwind scheme.

The viscous incompressible N-S equation (Laan *et al.* 2015, Li *et al.* 2016), the continuity

equation based on Reynolds average, and the momentum equation are as follows

$$\frac{\partial \mu_i}{\partial x_i} = 0 \quad (16)$$

$$\frac{\partial(\rho \overline{\mu_i})}{\partial t} + \frac{\partial(\rho \overline{\mu_i \mu_j})}{\partial x_j} = -\frac{\partial(\overline{p})}{\partial x_i} + \frac{\partial}{\partial x_j} \left(\mu \frac{\partial \overline{\mu_i}}{\partial x_j} - \rho \overline{\mu_i \mu_j} \right) \quad (17)$$

Where, $i, j=1,2$; $\rho=1.225 \text{ kg/m}^3$, which is the air density; $\mu=1.7894 \times 10^{-5} \text{ kg/(m}\cdot\text{s)}$, which is the dynamic viscosity coefficient.

$$\frac{\partial(\rho_m k)}{\partial t} + \frac{\partial(\rho_m k \mu_j)}{\partial x_j} = P - \rho_m \varepsilon + \frac{\partial}{\partial x_j} \left[\left(\mu + \frac{\mu_t}{\sigma_k} \right) \frac{\partial k}{\partial x_j} \right] \quad (18)$$

$$\frac{\partial(\rho_m \varepsilon)}{\partial t} + \frac{\partial(\rho_m \xi \mu_j)}{\partial x_j} = C_{\varepsilon 1} \frac{\xi}{k} P_t - C_{\varepsilon 2} \rho_m \frac{\xi^2}{k} + \frac{\partial}{\partial x_j} \left[\left(\mu + \frac{\mu_t}{\sigma_k} \right) \frac{\partial \xi}{\partial x_j} \right] \quad (19)$$

$$\mu_t = \frac{C_\mu \rho_m k^2}{\xi} \quad (20)$$

Where, k and ε are turbulent energy and turbulent dissipation rate, P_t is the turbulence energy generation term, μ_t is the turbulent viscosity coefficient. The model constants are $C_{\varepsilon 1}=1.44$, $C_{\varepsilon 2}=1.92$, $\sigma_\xi=1.3$, $\sigma_k=1.0$, and $C_\mu=0.09$.

On the basis of satisfying above quality and momentum conservation equations, the basic motion features of turbulence are described by using Eqs. (21)-(23), (Lee *et al.* 2015).

$$\frac{\partial H}{\partial t} + \frac{\partial(\mu H)}{\partial x} + \frac{\partial(v H)}{\partial y} + \frac{\partial(w H)}{\partial z} = 0 \quad (21)$$

$$\frac{\partial(\mu H)}{\partial t} + \frac{\partial}{\partial x} \left[u^2 H + \frac{1}{2} g H^2 \right] + \frac{\partial(\mu v H)}{\partial y} = H f v - g H \frac{\partial Z_b}{\partial x} - \frac{H}{\rho} \frac{\partial p}{\partial x} + \frac{\tau_{ax} - \tau_{bx}}{\rho} \quad (22)$$

$$\frac{\partial(v H)}{\partial t} + \frac{\partial(\mu v H)}{\partial x} + \frac{\partial}{\partial y} \left[v^2 H + \frac{1}{2} g H^2 \right] = -H f u - g H \frac{\partial Z_b}{\partial y} - \frac{H}{\rho} \frac{\partial p}{\partial y} + \frac{\tau_{ay} - \tau_{by}}{\rho} \quad (23)$$

Where, u , v , and w are the components of the velocity vector $u(z)$ in x , y , z directions; H is the calculation point height of the wind wheel; g is the gravitational acceleration; $f = 2w \sin \varphi$, w is the geostrophic angular velocity, φ is the geographic latitude of the calculation point; Z_b is the ground elevation; τ_{ax} and τ_{bx} are the stress components in the x and y directions; τ_{bx} and τ_{by} are the friction components of wind and rain in the x and y directions; p is the pressure difference; ρ is the air density.

The k - ε model is a turbulence calculation model with high Reynolds numbers and can well predict fully developed a turbulent flow. It is suitable for the simulation of flow fields around this kind of large-scale megawatt wind turbines (Ke *et al.* 2016).

Table 2 Calculation parameters and boundary conditions

Calculation parameters	Parameter settings	Calculation parameters	Parameter settings
Inlet boundary conditions	Velocity outlet	Other boundary conditions	Symmetrical boundary conditions
Outlet boundary conditions	Pressure outlet	Pressure term discretization	Standard format
Wall surface boundary conditions	Non-slipping wall surface	Convergence tolerance	10^{-6}

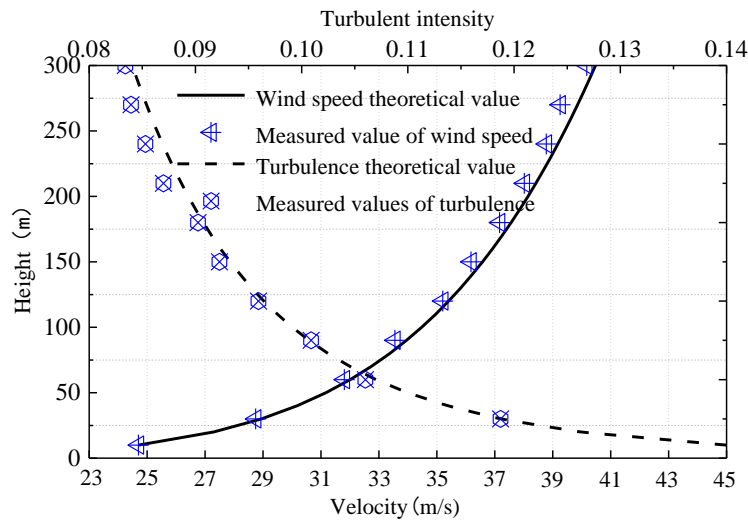


Fig. 5 Schematic of average wind speed profile and turbulence strength distribution

4.2.2 Inflow boundary setting

The wind speed profiles are compiled using user-defined functions. The blades are assumed to be rigid, and the surface of the wind turbine system is set as the non-slipping boundary condition. Symmetrical boundary conditions are set in the side faces and top faces of the flow field. The atmosphere boundary of the model top is set as the symmetrical boundary with zero slipping wall surface. Table 2 gives the detailed calculation parameters and boundary conditions of numerical simulation.

The inlet boundary is defined as the velocity inlet. The exponent wind profile and the turbulence degree profiles of the atmosphere boundary layer are set according to the B-type landform. Fig. 5 schematically shows the average wind speed profile and turbulence strength distribution. The ground roughness index in the wind profile is 0.15. The basic wind speed at the reference height of 10 m is 25 m/s, which corresponds to the cut-out speed of the wind turbine. The UDF (user-defined function) is utilized to realize the connection between the inlet boundary conditions and FLUENT. Detailed implementation methods can be found in Refs. (Ke *et al.* 2016, Ke *et al.* 2016).

4.3 Validation of effectiveness

The surface pressure coefficient of wind turbine tower is the evaluation key index of aerodynamic performance (Ke *et al.* 2016). The numerical simulation results are substituted into Eqs. (24) and (25), and transformed, with the calculation results compared with standard curves (GB 50009-2012).

$$C_{pi} = \frac{P_i - P_H}{0.5\rho V_H^2} \quad (24)$$

Where C_{pi} is the average wind pressure coefficient at Point i ; P_i is the average pressure of the measured point; P_H is the pressure far ahead of the reference height; ρ is the air density and set as 1.225 kg/m^3 ; V_H is the average wind speed far ahead of the reference height.

$$\mu_{si} = \frac{C_{pi}}{\mu_{zi}} \mu_{zr} = C_{pi} \left(\frac{Z_r}{Z_i} \right)^{2\alpha} \quad (25)$$

Where C_{pi} is the average wind pressure at Point i ; μ_{zi} and μ_{zr} are the height variation coefficients of wind pressure at Point i and the reference height; Z_i is the distance between Point i and the basement; Z_r is the reference height; α is the ground roughness coefficient.

By transforming the pressure coefficient at each point into the shape factor, Fig. 6 gives the circumferential distribution of shape factors of the tower at the height of 30 m under eight working conditions. Based on the comparison, it can be found that angles corresponding to the extreme points and separation points of the negative pressure in the average wind pressure coefficient distribution curves under different working conditions are consistent with those in standard curves. The values of wind pressure coefficients in the windward and crosswind regions agree well. Only in the leeward region, the negative pressure coefficient is lower than the standard value. The comparison results validate the effectiveness of numerical simulation.

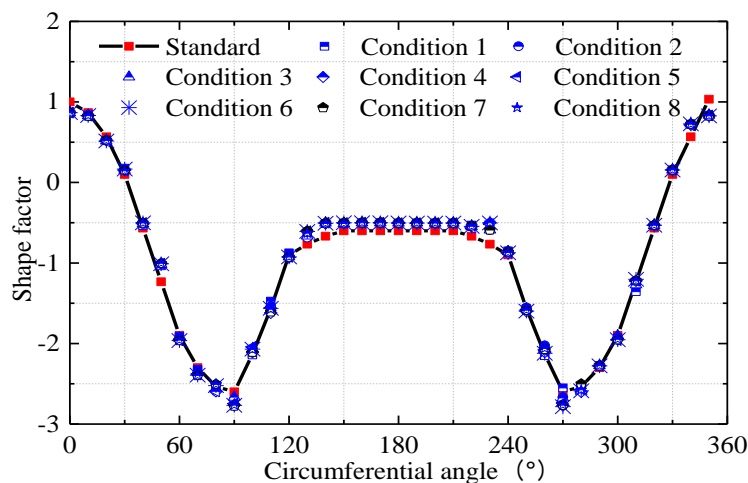


Fig. 6 Comparison of numerical simulation results and standard curves

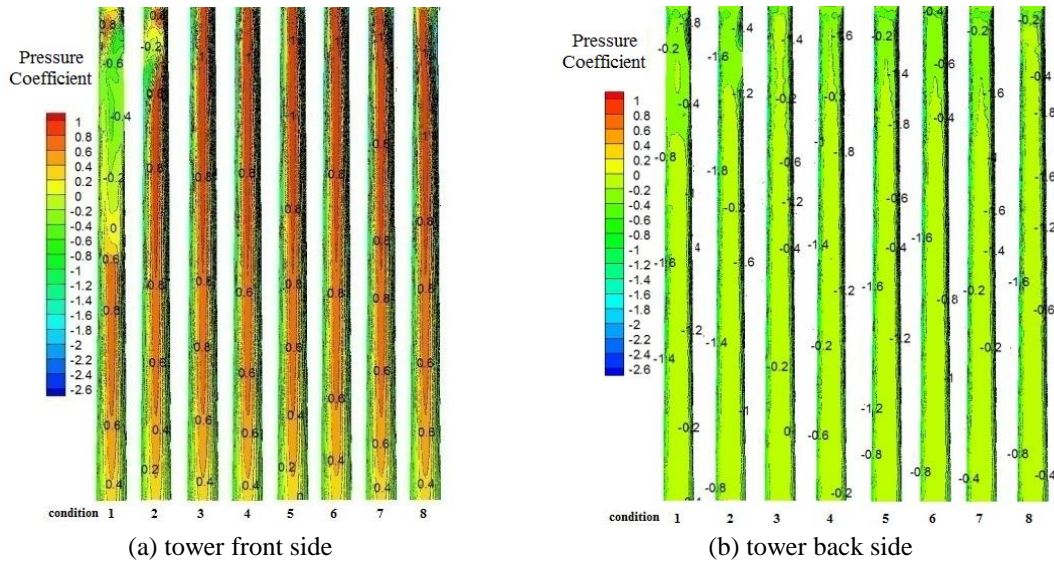


Fig. 7 Contour maps of tower pressure coefficients under different working conditions

4.4 Numerical simulation results

4.4.1 Average wind pressure coefficient

Fig. 7 gives the contour maps of tower pressure coefficients under eight working conditions. As shown in the color bar of the figure, the blue represents the negative value, and the red represents the positive value. When negative values tend to be positive, blue is gradually shifting to red. In Fig. 5, "color bar" lists the representative color of pressure value from -2.6 to +1. Therefore, it is known that the front of the tower is mostly a red area, that is, the pressure coefficient is positive, and the back of the tower is mostly bluish green, that is, the pressure coefficient is negative. Via comparison, it can be found that: 1) the shielding effect of the blade on the tower significantly affects the positive pressure distribution in the windward side of the tower. In the shielded region, obvious negative pressure distribution bands occur, which gradually disappear with the decrease of shielding area; 2) under the working condition when the tower is not shielded by blades along the incoming flow direction, long and narrow positive pressure distribution regions occur in the windward side of the tower, with almost similar pressure distribution conditions; 3) due to the influence of the blade shielding effect, the absolute value of negative pressure region in the top part of the tower leeward side under Working condition 1 is obviously higher than those under working conditions unaffected by blade, and the absolute value gradually decreases with the reduction of shielding effect.

Fig. 8 gives the contour maps of pressure coefficients of three blades under different working conditions. As shown in the color bar of the figure, the blue represents the negative value, and the red represents the positive value. It is implied that: 1) the wind pressure values in windward sides of three blades under different working conditions are all positive, with local negative pressure regions distributing in the blade root; 2) the upwind turbine blade is not hindered in the incoming flow direction, leading to the similar distribution of positive pressure in the windward side of each blade under different working conditions. But the distribution region of positive pressure in the

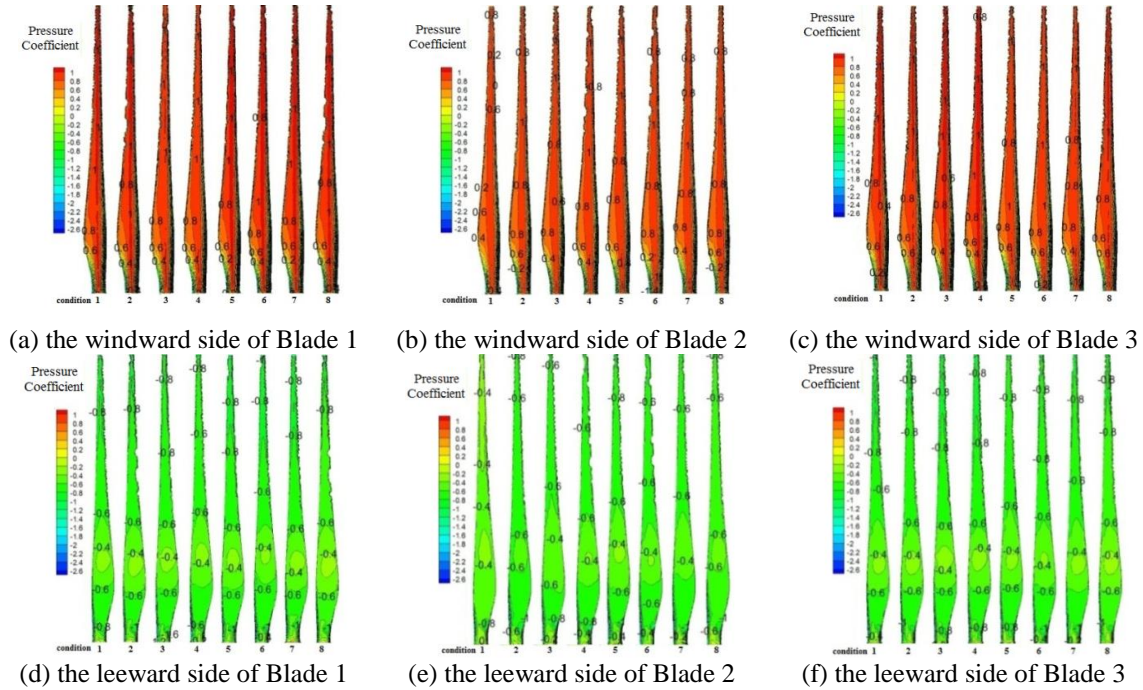


Fig. 8 Distribution contours of blade pressure coefficients under different working conditions

blade root of working condition slightly differs from other working conditions; 3) the shielding effect of the blade-tower coupled system has a significant influence on the pressure values of blade leeward side. The Blade 2 presents a negative pressure distribution different from those of Blade 1 and Blade 3. At two blade positions corresponding to Working condition 2, the negative pressure values are around -0.6 and -0.4, respectively. The pressure coefficient in the blade tip is smaller than those of Blade 1 and Blade 2, with a value of -0.6.

4.4.2 Vorticity distribution

Fig. 9 gives the x-z horizontal mean vorticity contours of the tower-blade coupled system under eight working conditions. As color bar shows, when blue is gradually transiting to green and then red, the value increases. Based on the comparison, following conclusions can be drawn:

1) the disturbance of blade on the tower mainly presents via the proximity effect. In the leeward side of Blade 1, a free shear layer adhering to the tower windward side exists in the leeward side of Blade 1, and the adhering area gradually decreases with the reduction of shielding area;

2) air flow adhering to the tower windward side presents a single bluff body streaming phenomenon, with mature vortex separation in the upper part of the tower leeward side. Under Working condition 1, when Blade 1 completely overlaps with the tower, the separation phenomenon is most obvious;

3) the shear layer adheres to the leeward side of the upper blade. The wake flow fully develops into an obvious vortex separation flow state and strikes the cabin back and top, forming small pressure concentrated zones. With the wind load vertical height of the upper blade increasing, this phenomenon becomes more obvious.

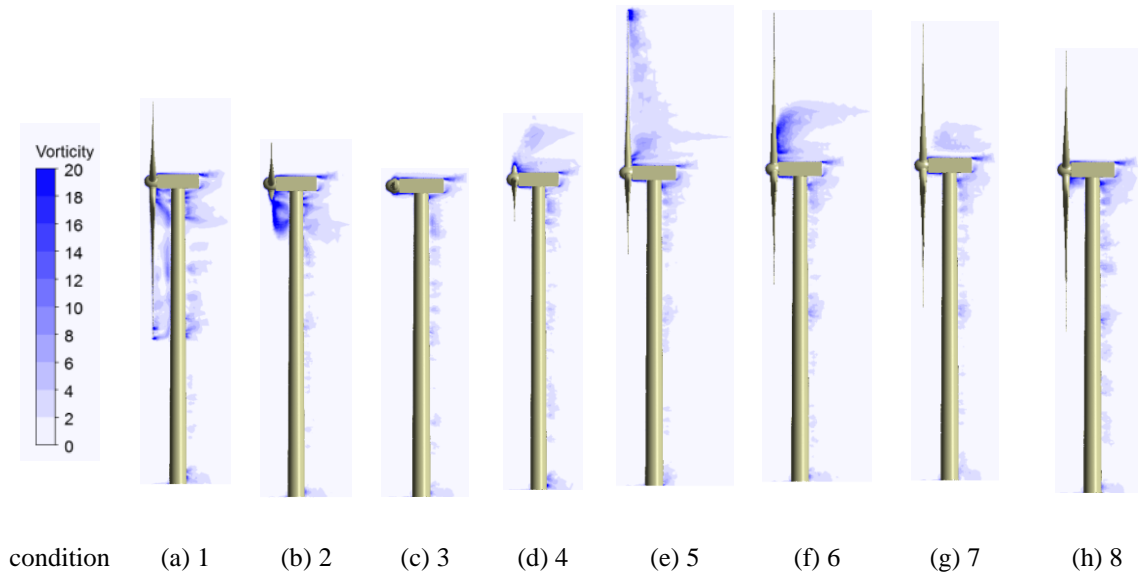


Fig. 9 The x-z horizontal mean vorticity distribution of the wind turbine system under different conditions

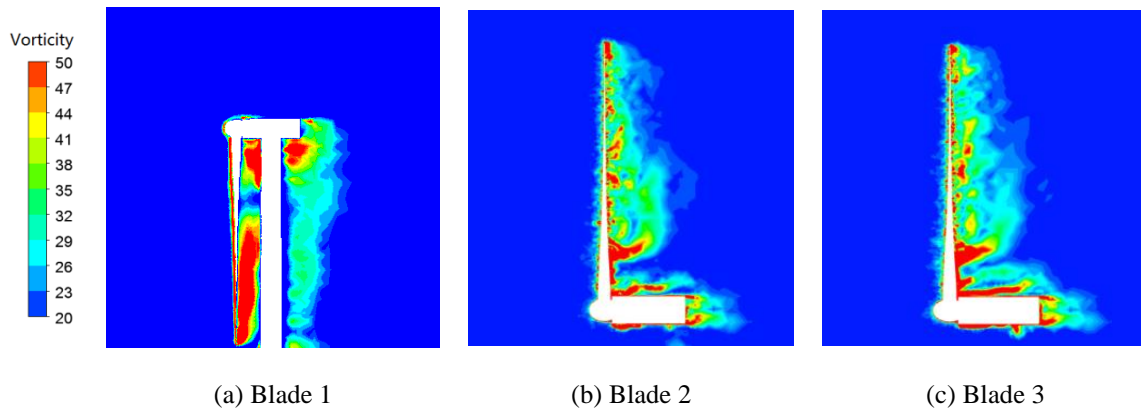


Fig. 10 Vorticity distribution of different blades under Working condition 1

Based on above analysis, it can be found that the aerodynamic performance of the tower-blade coupled system under Working condition 1 is poorer than those under other working conditions. Hence, Fig. 10 gives the vorticity distribution of three blades under Working condition 1, so as to further investigate the aerodynamic performance around the blade. Via comparison, it is implied that: obvious blade tip vortex and blade root vortex occur in the wake flow field of the blade, while blade trailing edge vortex also takes place between the blade root and blade tip; since the blade overlaps with the tower under this working condition, the area of blade tip vortex and blade root vortex is obviously greater than those of Blade 2 and Blade 3.

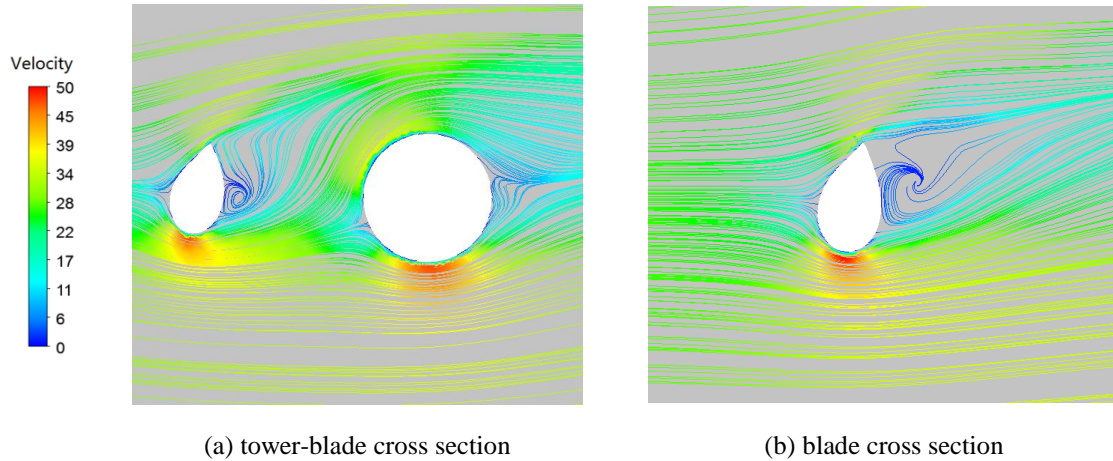


Fig. 11 Flow patterns of typical cross sections of the wind turbine system

4.4.3 Flow field analysis

Fig. 11 gives the speed flow patterns of typical cross sections of the wind turbine system. As color bar shows, when blue is gradually transiting to green and then red, the value increases. It is implied that the incoming flow experiences flow separation due to the resistance of blade. The separated flow adheres the blade surface. After passing the blade leading edge and blade trailing edge, the incoming flow forms vortices in the blade leeward side, with small side vortex forming near the blade surface; when the distance between the tower and blade is close enough, the vortex moves between the blade leeward side and tower windward side, resulting in negative pressure occurring in the tower windward side under working conditions 1 and 2. This phenomenon agrees well with the vortex distribution around the wind turbine system.

4.4.4 Distribution characteristic of rise drag coefficient

The interference effect between the blade and the tower will make the pressure distribution of the tower surface different, which makes the lift and drag coefficient difference at different heights of the tower. In order to analyze the influence of interference effect on the lift and drag coefficient of the tower, Table 3 gives a list of the lift and drag coefficient of the tower under different working conditions. Due to the same distribution of the lift and drag coefficient of the three blades, Table 2 gives a list of lift and drag coefficients only by blade 1. From table 3 and table 4: 1) the lift coefficient of the undisturbed section of the tower is basically less than the drag coefficient. It is showed that the pressure coefficient of the undisturbed section presents a symmetrical distribution making the sum of drag coefficient and the lateral lift coefficient offset; 2) the influence of blade wake on the tower makes the distribution of pressure coefficient distribution on the surface of the tower change. There is a phenomenon that the drag coefficient is less than the lift coefficient at the height above 40m of the tower under eight conditions; 3) with the influence of interference, the lift coefficient is larger than the drag coefficient from 1 to 3. In addition, the lift coefficient decreases gradually as the blade rotates away from the tower.

Table 3 The list of lift and drag coefficient at typical height of tower under different conditions

Condition		1	2	3	4	5	6	7	8
undisturbed	C_d	0.409	0.455	0.622	0.403	0.514	0.363	0.382	0.323
region	C_l	-0.035	-0.032	-0.037	-0.107	0.104	0.049	0.052	0.019
disturbed	C_d	0.167	0.298	0.393	0.345	0.336	0.336	0.323	0.290
region	C_l	0.309	-0.126	-0.137	-0.082	0.030	0.030	-0.149	-0.038

Table 4 The list of lift and drag coefficient of blade 1 under different conditions

Condition	1	2	3	4	5	6	7	8
C_d	0.237	0.215	0.195	0.207	0.224	0.261	0.280	0.286
C_l	0.322	0.318	0.214	0.105	0.037	-0.113	-0.126	-0.147

5. Aerostatic response analysis

5.1 Finite element modeling and dynamic characteristics

The finite element models of the tower-blade coupled system under different working conditions were constructed based on ANSYS. The tower and blades were meshed with Shell63 elements. The cabin was meshed with Beam188 beam elements, with its internal structure ignored. The mesh type of the round raft base was Solid65, with a diameter of 24 m and a height of 2 m. The base bottom was fixed, and the interaction between the base and ground was simulated using Combin14 spring elements.

The dynamic characteristic which can know the vibration frequency and mode react the inherent dynamic performance of the structure. According vibration frequency and mode can reduce the interference effect which produced the dynamic load on the structure.

In this paper, the dynamic equilibrium equation of the structure is solved, and assumed that the structure is not subjected to external force.

$$[M]\{\ddot{u}\} + [C]\{\dot{u}\} + [K]\{u\} = 0 \quad (26)$$

Suppose that its solution is

$$\{x\} = \{\psi\} e^{\lambda t} \quad (27)$$

Put it in the above equation

$$(\lambda^2[m] + \lambda[c] + [k])\{\psi\} = [D(\lambda)]\{\psi\} = \{0\} \quad (28)$$

$[D(\lambda)]$ is the characteristic matrix of the system. The above formula belongs to the two eigenvalue. The necessary and sufficient conditions for the existence of the nonzero solution are shown as follows.

$$| [D(\lambda)] | = | \lambda^2 [m] + \lambda [c] + [k] | = 0 \quad (29)$$

The above formula is a $2n$ algebraic equation of λ with $2n$ characteristic root $\lambda_i (i=1,2,\dots,2n)$. Usually, λ_i is a complex number. Due to the positive definiteness of the damping matrix, and the mass matrix, the stiffness matrix and the damping matrix are the real matrix. Therefore, the λ_i must have the negative real part, and are conjugated in pairs. The eigenvectors corresponding to the complex eigenvalues are also conjugated plural forms. Based on the above calculation principle, the more accurate and faster Block Lanczos method is used to analyze the dynamic characteristics. Please refer to the revised draft for details.

Fig. 12 gives the distribution of the first 100 order natural frequencies. For Working condition 1, Fig. 10 shows its natural frequency values, while for other working conditions, only the add/reduce values comparing to Working condition 1 are shown. It is demonstrated that the structure fundamental frequency of Working condition 1 is obviously lower than other working conditions. With the area of the tower shielded by blades decreasing, the fundamental frequency gradually increases. Among them, the overall structure fundamental frequency of Working condition 5 is the greatest. The rotation of blade position has an obvious influence on the low order frequency of the wind turbine system, while has limited influence on the high order frequency.

Hence, it can be found that the blade shutdown position has an insignificant influence on the frequency of wind turbine, and only Working condition 1 is taken to give the typical vibration modes of the wind turbine. As demonstrated in Table 5, the low order vibration modes are mainly the back-forth waving and left-right oscillating of the blade, cabin and tower. With the increase of fundamental frequency, the blade waving becomes more obvious, and the structure deformation and instability configuration of tower and blade occur in high order modes.

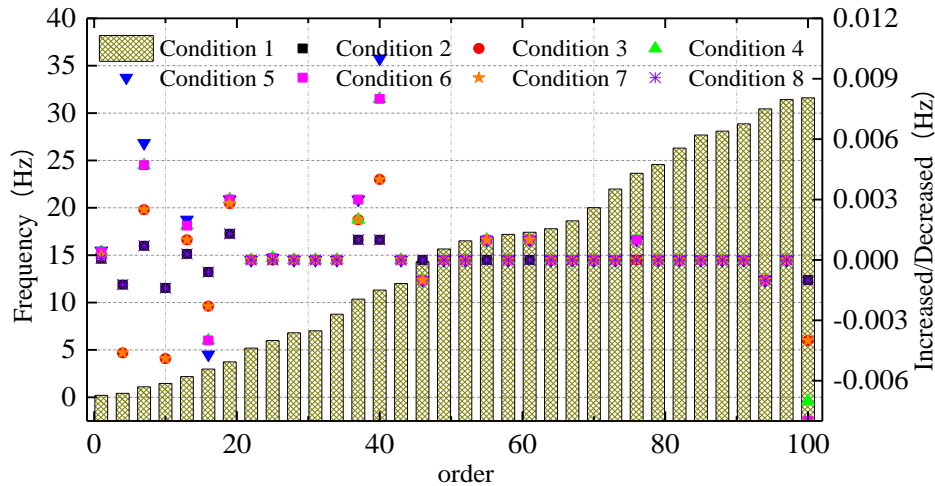
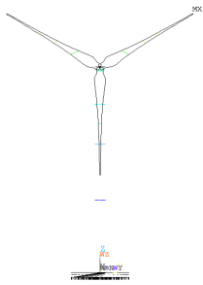
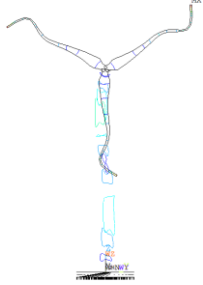
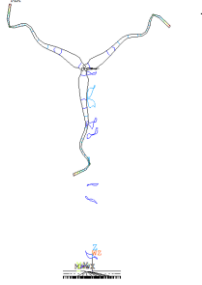
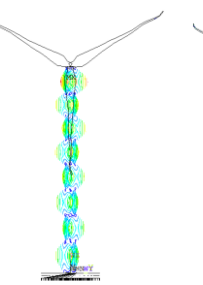
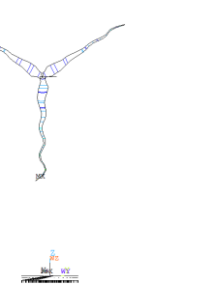


Fig. 12 Illustration of the first 100 order natural frequencies of the wind turbine under different working conditions

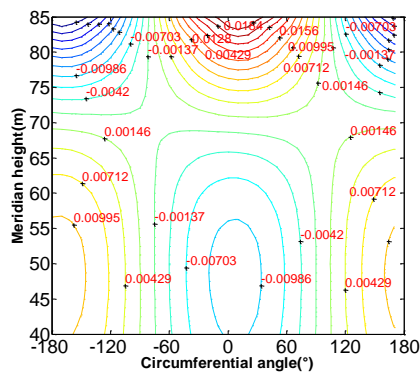
Table 5 Typical vibration modes of the wind turbine

Orders	1,2	35,36	49,50	79,80	99,100
Natural frequency	0.21	8.92	16.01	24.56	31.61
Vibration modes					

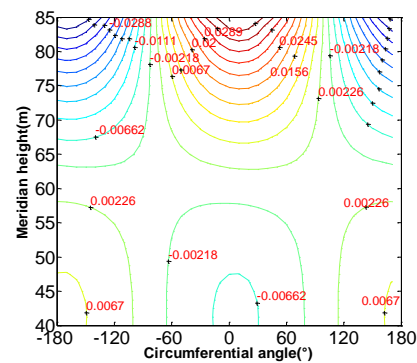
5.2 Wind-induced response

5.2.1 Tower response

Fig. 13 gives the 3D schematic diagrams of the radical displacement of typical sections of the tower under different working conditions. As shown in the figure, under working conditions when the blades have shielding effects on the tower, the tower radical displacement is obviously greater than those without shielding. For Working condition 4, when the shielding effect does not exist, the tower radical displacement is the greatest. Due to the influences of the blade root disturbance and the tower-blade coupling effect, obvious demarcation points exist at the tower radical displacement of 70 ± 5 m under various working conditions. With the shielding area of blade root on the tower decreases, the contour lines of radical displacement become denser.



(a) Working condition 1



(b) Working condition 2

Continued--

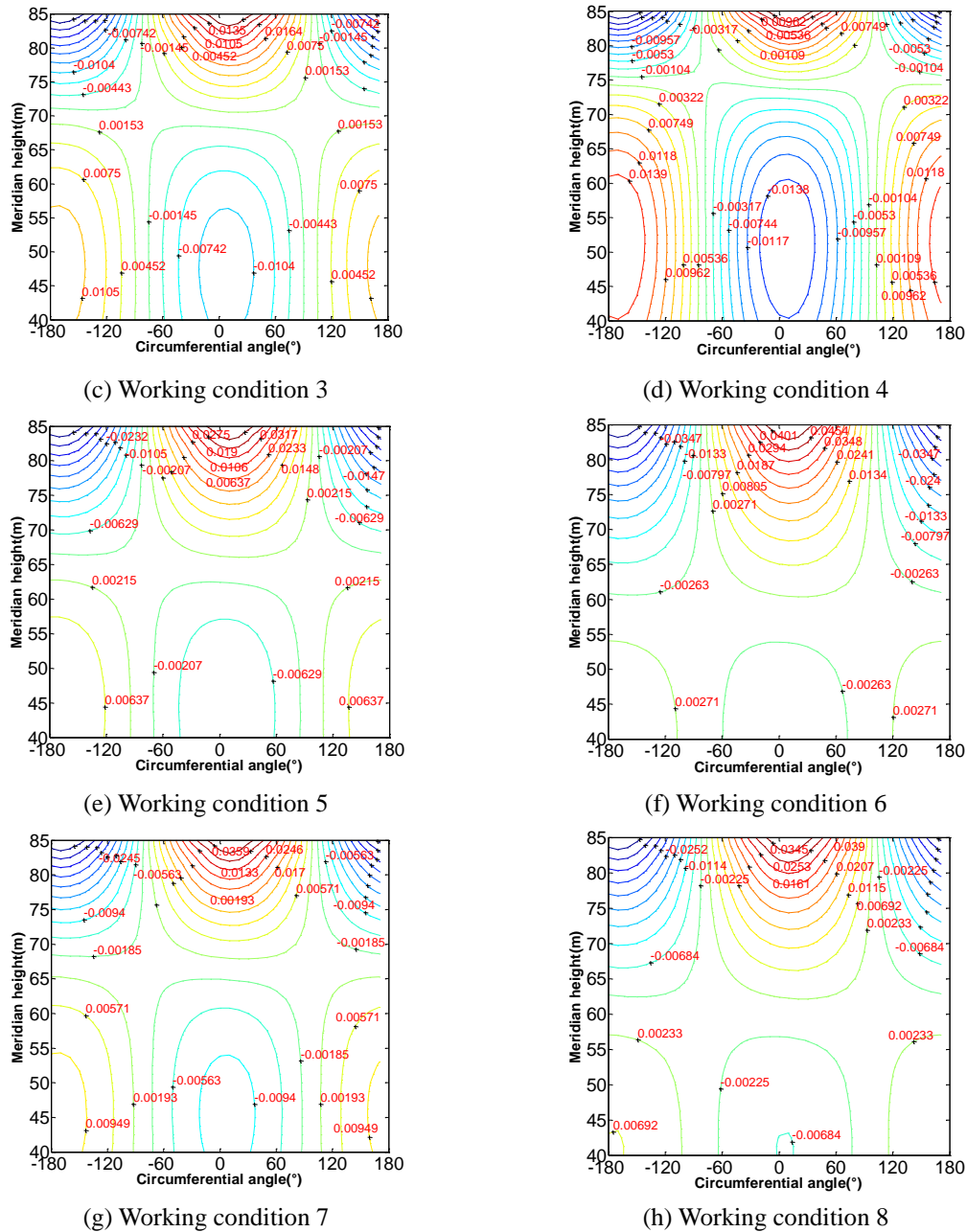


Fig. 13 3D diagrams of the radical displacement of typical sections of the tower under different working conditions

To further analyze the influence of blade shutdown position on the wind-induced response, Fig. 14 compares the circumferential moment values at typical heights of the tower under different working conditions. For Working condition 1, its moment value is fully displayed, while for the

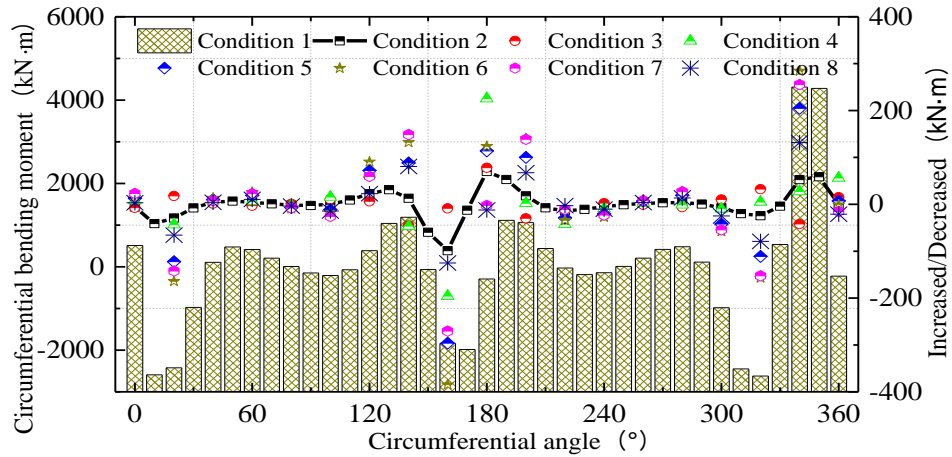


Fig. 14 Comparison of the circumferential moment at typical heights of tower disturbance regions under different working conditions

other working conditions, only the add/reduce values comparing to Working condition 1 are shown. Via comparison, it can be found that, the circumferential moment at this height does not present a symmetrical distribution with the windward side as the center, instead, its symcenter locates at the left side of the windward side with an angle of 15° and no moment mutation exists at this point. The shielding effect of the blade on tower obviously affects the moment values in the crosswind and leeward sides of the tower, and its value increases with the reduction of shielding area. For Working condition 6, when the tower is not shielded by blades, the value variation amplitude is obvious.

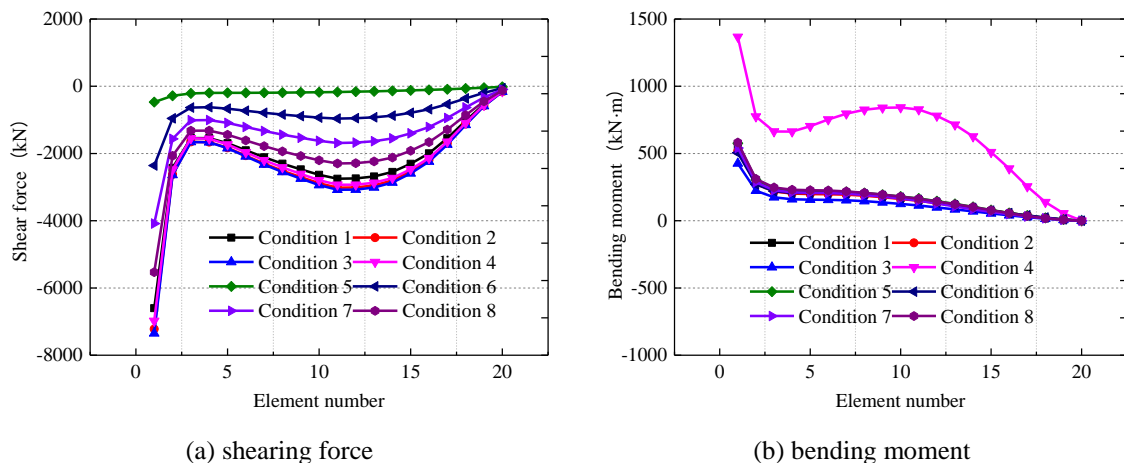


Fig. 15 Comparison of blade shearing force and bending moment under different working conditions

5.2.2 Blade response

Fig. 15 compares the shearing force and bending moment of Blade 1 under different working conditions. The element No. 1 is defined as the blade root. It is demonstrated that: 1) the internal force of blade root is the greatest under all working conditions. The shearing force and bending moment present a tendency of first-decrease-then-increase from the blade root to the blade tip; 2) the shielding effect of the blade on the tower has an obvious influence on the blade shearing force, but doesn't presents an obvious variation tendency. For Working conditions 1-4, when the shielding effect exists, the blade shearing force is relatively great. For Working condition 5, when the tower is not shielded by blades, the blade shearing force is the smallest; 3) the bending moment of Blade 1 differs little, while the bending moment of Working condition 4 is the greatest, with the maximum shearing force in the blade root being 50% greater than that of Working condition 3.

6. Analysis of wind-induced stability performance

6.1 Geometrical nonlinearity

Fig. 16 shows the maximum structure displacement curves of linear and nonlinear analyses of the tower-blade coupled system of the wind turbine. Based on the comparison, it is demonstrated that: 1) the variation regularities of structure displacement under both linear and nonlinear analyses are similar. But, with the reduction of the blade shielding effect on the tower, the structure displacement doesn't present a similar variation regularity. The displacement values can be ranked as follows: Working condition 1 > Working condition 8 > Working condition 4 > Working condition 7 > Working condition 3 > Working condition 2 > Working condition 6 > Working condition 5; 2) the geometrical nonlinearity has different influences on the maximum displacement of the wind turbine system at different shutdown positions. That is, it decreases the maximum displacement values of Working conditions 4, 5, 6, and 7, which all have weak shielding effects, while increases the maximum displacement of working conditions with strong shielding effect; 3) the nonlinearity has slight influence on the maximum displacement, with a maximum deviation of only 0.04.

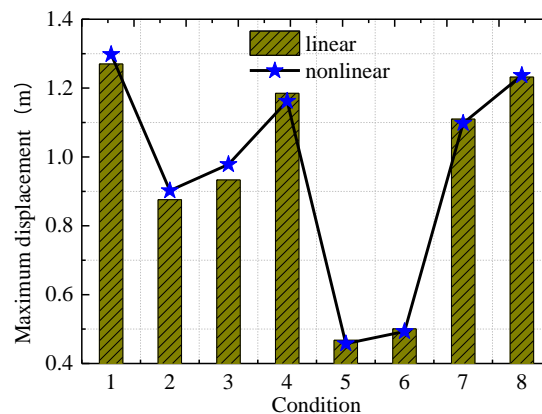


Fig. 16 Comparison of the maximum displacement of wind turbine system under different working conditions with basic wind speed (considering linearity and nonlinearity)

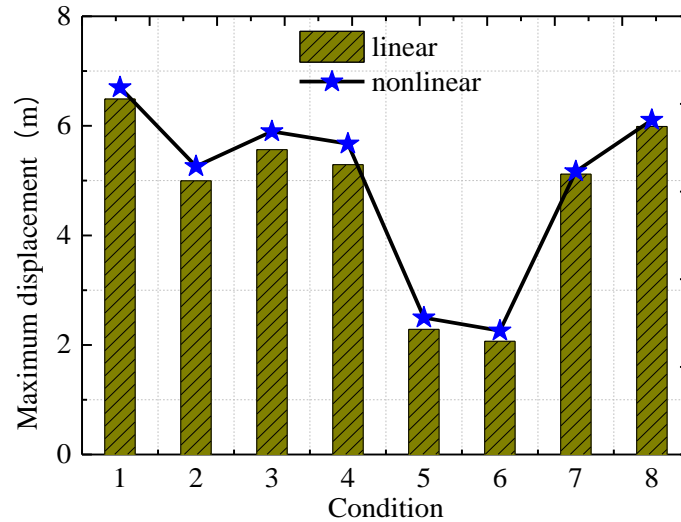


Fig. 17 Comparison of the maximum displacement of wind turbine system under different working conditions with buckling wind speed (considering linearity and nonlinearity)

To further reveal the variation behavior of wind-induced response with wind pressure during the geometrically nonlinear analysis of the wind turbine system, the maximum displacement variation curves of wind turbine systems considering geometrical nonlinearity are obtained by applying corresponding buckling wind speed according to buckling coefficients related to different working conditions. According to Fig. 17, considering geometrical nonlinearity under the buckling speed obviously changes the distribution regularity of wind-induced maximum displacement. Moreover, the maximum displacement values obtained via nonlinear analyses under eight working conditions are all greater than those obtained via linear analyses. The comprehensive analysis results indicate that, considering geometrical nonlinearity has very limited influence on the maximum structure displacement. Hence, it can be ignored during structure design.

6.2 Buckling stability

Fig. 18 compares the first 10 order buckling loading factors under eight working conditions. Via comparison, it can be found that: 1) the structure buckling factors under all working conditions are greater than 1. Hence, the blade doesn't completely buckle under the rated wind speed, and the buckling factor increases with the rising of order; 2) the shielding effect of blades on the tower has a significant influence on the buckling factor. With the reduction of shielding effect, the buckling factor gradually decreases, and the deviation of buckling factors under different working conditions also increase with the increase of order.

Table 6 lists the buckling modes of typical orders of the wind turbine system at eight shutdown positions. The ones labeled by black rectangles are the most unfavorable modes. The results indicate that: the buckling energy of this system mainly concentrates in low orders and the overall structure vibration modes are complicated. Accompanied with back-forth and left-right swinging, the tower and blades present obvious 3D features. With the reduction of blade shielding area, the

low order vibration modes become more complex, mainly manifesting as the tower top deformation gradually increases. In the base order vibration mode, the buckling mode of Working condition 8 is the most unfavorable among all eight working conditions. Working conditions 4 and 5 are the most unfavorable ones among high-order vibration modes. This phenomenon indicates that the reduction of shielding effect enlarges the buckling displacement, which further promotes the buckling instability of structures.

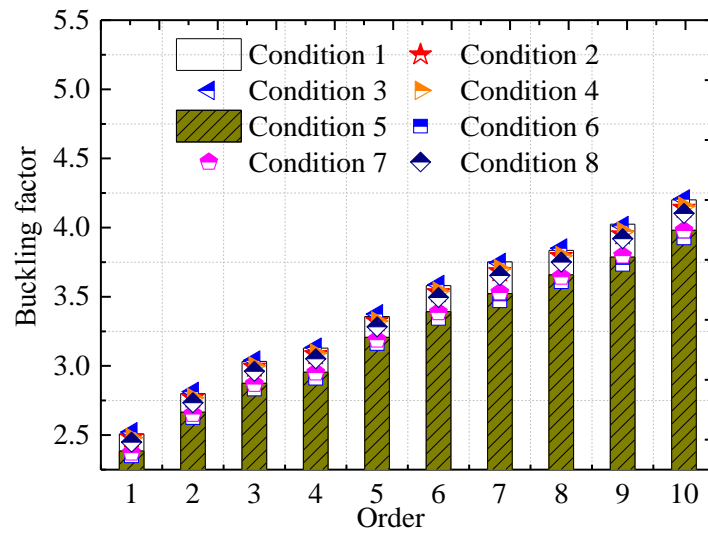


Fig. 18 First 10 order buckling loading factors under different working conditions

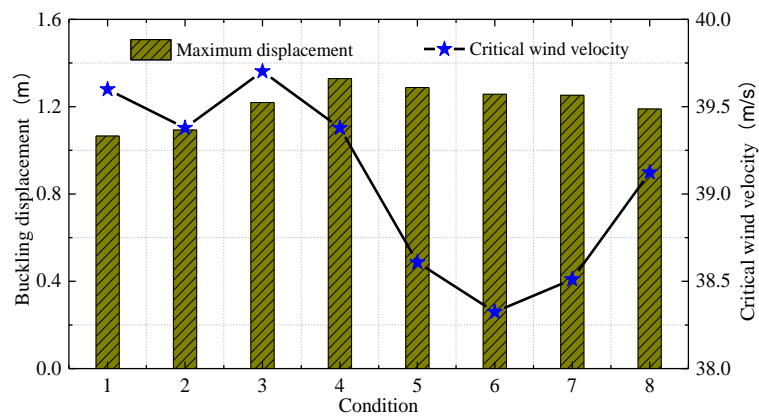


Fig. 19 Schematically comparison of the buckling displacement and critical wind speed of the tower-blade coupled system under different working conditions

Table 6 Typical order buckling modes of the wind turbine under different working conditions












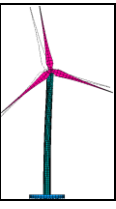






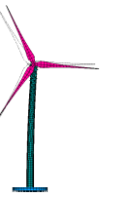

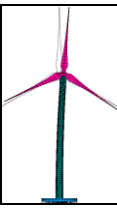





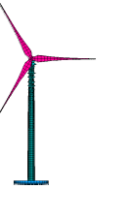

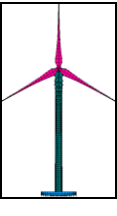





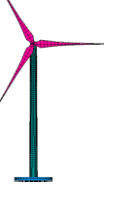
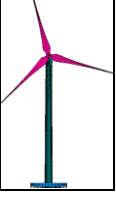




order	condition							
	1	2	3	4	5	6	7	8
1 , 2								
3 , 4								
25 , 26								
33 , 34								
49 , 50								

Fig. 19 schematically compares the buckling displacement and critical wind speed of the tower-blade coupled system under different working conditions. It can be found that: 1) the blade shutdown position has a significant influence on the buckling displacement of the overall structure during buckling. With the area of tower shielded by blades reducing, the displacement slowly increases, and reaches its maximum value under Working condition 4, when the blades have no shielding effect on the tower; 2) with the shielding effect of blades on the tower decreasing, the critical wind speed presents different variation regularities. However, the structure critical wind speed under working conditions when the tower is shielded by blades is obviously greater than those not shielded. Under working condition 6, when the tower is completely not shielded by blades, the critical wind speed reduces to the minimum value among all eight working conditions. By summarizing the influences of buckling displacement and critical wind speed on the buckling stability performance of the wind turbine system, it can be found that the buckling stability of Working condition 3 is the best, while the blade position in working condition is the shutdown position most easily for buckling instability to take place.

6.3 Ultimate bearing capacity

To further characterize the influences of parameters including aerostatic instability mode and instability wind speed on the wind-induced ultimate bearing capacity of wind turbine systems (Wang and Cheng 2015, Ding *et al.* 2015, Sun *et al.* 2015, Plaza *et al.* 2015), analyses were conducted as follows: with the initial wind speed of 25 m/s at the height of 10 m as the basis, the wind speed is increased step-by-step, with wind speed loading step of 1 m/s~10 m/s. The gradient of the maximum deformation displacement changing with wind speed is utilized to determine the ultimate bearing state, with specific implementation modes listed in Fig. 20.

Fig. 21 shows the variation of wind turbine displacement changing with wind speed under different working conditions. Via comparison, it can be found that: 1) with the step-by-step loading of wind speed, the maximum structure deformation under eight working conditions all first increases, then sharply decreases and finally increases with small amplitudes; 2) the blade shutdown position significantly changes the wind speed corresponding to the sharp reduction of structure deformation (for the convenience of description, the wind speed at the sharp reduction point is defined as the critical wind speed in following discussions), and decreases with the shielding area reducing. Meanwhile, under Working conditions 4, 5, and 6, when the tower is completely not shielded by blades, the critical wind speeds are all greater than that under Working condition 1; 3) the maximum displacement under each working condition is seriously affected by the blade shutdown position. In the rising stage before the sharp reduction of maximum displacement, the maximum displacement also decreases with the reduction of shielding area. However, for the maximum displacement of working condition 4 when it is completely not shielded by blades, its value in the rising stage is obviously higher than those under other working conditions. The maximum displacement value reaches the largest value in the rising stage after the sharp reduction under working condition 1 when Blade 1 fully overlaps the tower.

To further analyze the mechanism of the first increasing and then sharply decreasing variation behavior of the maximum displacement during wind speed increasing, Working condition 1 is taken as an example to give the buckling modes and press-velocity curves under wind speeds corresponding to those before and after the sharp reduction of the overall structure deformation. As color bar shows, when blue is gradually transiting to green and then red, the value increases. It can be implied that: 1) when the wind speed reaches the critical value, the tower deformation pattern

mutates from leaning back to bending forward, and the lower blade also mutates from getting far away from the tower to getting close to the tower. The swinging of upper blade presents obvious 3D features, accompanied by a tendency of getting far away from the tower; 2) when the wind speed is gradually increased to the critical speed value, the positive pressure values of the lower blade and tower windward side both increase noticeably, while the negative pressure of the upper blade also rises, resulting in the anticlockwise swinging of blades parallel to the tower direction; 3) the incoming flow separates in the windward side due to the blade shielding effect. Some air flow in the blade tip climbs upward due to tower shielding and combines with the air flow separated from the upper blade root, forming converse vortex separation and narrow negative pressure value-added region in the area shielded by tower and blades. In addition, small vortexes are formed in the tower leeward side by air flow separated along the tower crosswind region. Vortex separation in local regions leads to the windward reverse deformation of the tower. Hence, it is indicated that when the wind speed increases to a certain critical value, the blade introduces a reverse effect on the tower. This effect can decrease the windward deformation of the tower during the continuous increase of critical wind speed. With the reduction of tower area shielded by blades, the reverse effect becomes more obvious.

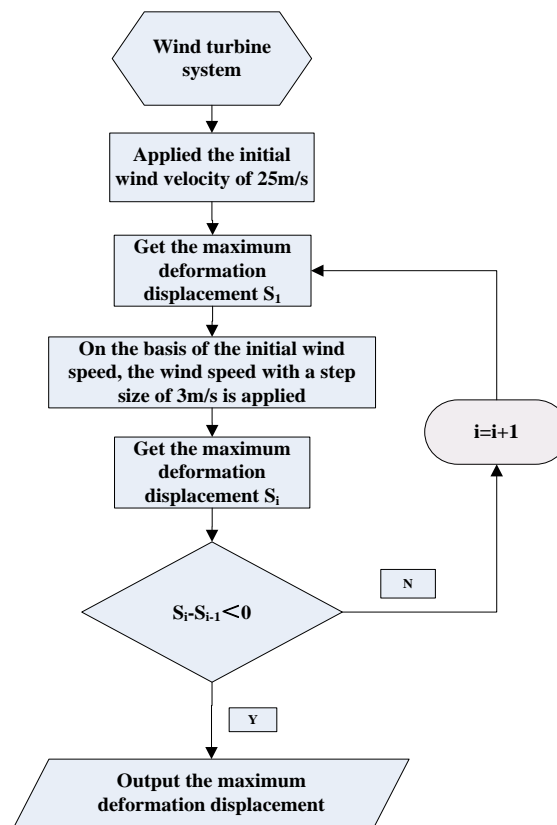


Fig. 20 Calculation flowchart of ultimate bearing capacity

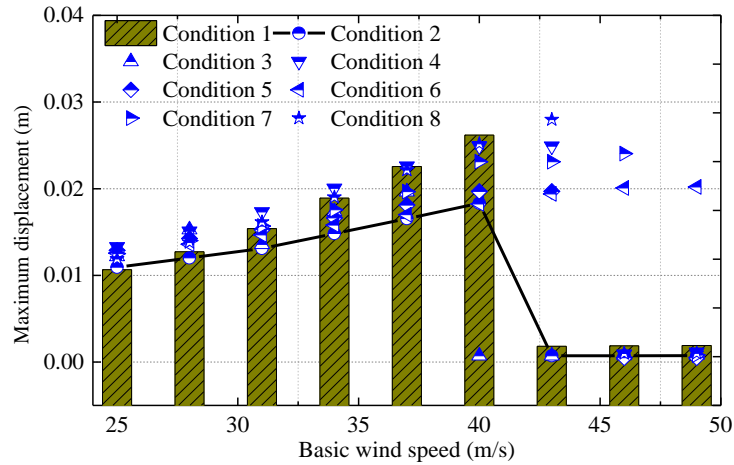


Fig. 21 Variation of wind turbine displacement changing with wind speed under different working conditions

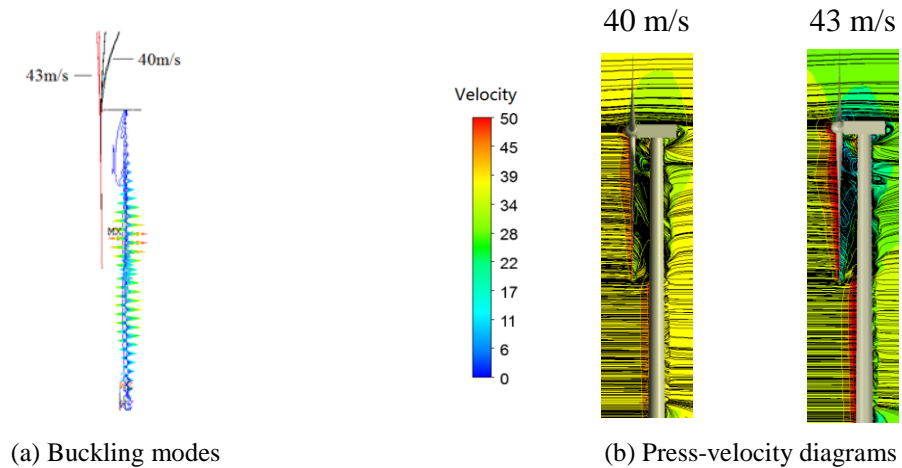


Fig. 22 Buckling modes and press-velocity diagrams before and after the sharp reduction of structure deformation under Working condition 1

According to the principle of equivalent balance force, the wind load applying on the blade is equalized to the tower top. That is, the concentrated force F and concentrated moment M both apply on the tower top. The moment on the tower top caused by the load of the upper two blades is greater than that caused by the lower blade. However, when the wind speed exceeds a certain value, the moment applied by the lower blade on the tower increases significantly and exceeds the value of upper blades. Detailed equalized results are shown in Fig. 23. The calculation results indicate that the tower top displacement caused by the concentrated force applying on the tower is smaller than that caused by the concentrated moment. Under the combined influence of these two actions, the final displacement of the tower top is bending forward. This is the beneficial effect caused by the coupling effect of tower-blade on the wind-induced stability of the wind turbine system.

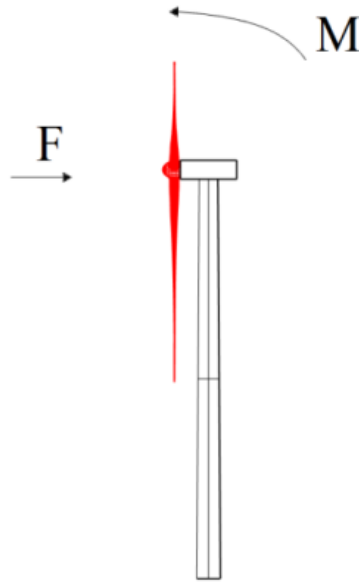


Fig. 23 Calculation diagram of the equivalent force of the wind turbine system

7. Conclusions

This paper comprehensively investigated the aerostatic response and stability performance of the tower-blade coupled system of wind turbine considering blade shutdown position. The main contents of this paper include aerodynamic performance, dynamic property, aerostatic response, geometrical nonlinearity, buckling stability and ultimate bearing capacity. Following conclusions can be drawn:

- In a rotation period of wind turbine blade, the system has the lowest fundamental frequency under working condition 1. With the area of tower shielded by blades decreasing, the system fundamental frequency gradually increases, with that under Working condition 5 becomes the largest. The blade position has an obvious influence on the low order frequency of the tower-blade system, while shows limited influence on the high order frequency.
- When the blade completely overlaps the tower (working condition 1), the aerodynamic performance of the system is the poorest while the aerostatic response is relatively small. Since the influence of the structure geometrical nonlinear on the system wind-induced response is small, the maximum displacement only has a discrepancy of 0.04. With the blade rotating clockwise, its wind-induced stability performance presents a variation regularity of first-increase-then-decrease. Under working condition 3, the critical instability wind speed reaches the maximum value, while the critical instability wind under working condition 6 is the smallest.
- The coupling effect between wind turbine tower and blade leads to a reverse effect which can significantly improve the ultimate bearing capacity of the system. With the reduction of the area of tower shielded by blades, this reverse effect becomes more obvious.

Therefore, it can be concluded that the blade shutdown position significantly affects the dynamic property, wind load, wind-induced stability, and ultimate bearing capacity of the wind

turbine system. The conclusions of this study can provide scientific references for the refined wind-resistance design of wind turbines under similar extreme working conditions.

Acknowledgments

This work was jointly funded by the National Natural Science Foundation of China (U1733129), NSFC-RGC cooperative research project of National Natural Science Foundation (51761165022), National Basic Research Program of China ("973" Program) under Grant No. 2014CB046200, open fund for Jiangsu Key Laboratory of Hi-Tech Research for Wind Turbine Design (ZAA1400206), Jiangsu province Qinglan Project, Six talent peaks project in Jiangsu Province (JZ-026) and China Postdoctoral Science Foundation (2015T80551).

References

- Arani, M.F.M. and Mohamed, A.R.I. (2015), "Analysis and impacts of implementing droop control in DFIG-based wind turbines on Microgrid/Weak-Grid stability", *IEEE T. Power Syst.*, **30**(1), 385-396.
- Ding, H., Liu, Y., Zhang, P. and Le, C. (2015), "Model tests on the bearing capacity of wide-shallow composite bucket foundations for offshore wind turbines in clay", *Ocean Eng.*, **103**, 114-122.
- Djojodihardjo, H., Hamid, M.F.A., Jaafar, A.A., *et al.* (2013), "Computational study on the aerodynamic performance of wind turbine airfoil fitted with Coanda", *Renew. Energ.*, **2013**.
- GB/T 20319-2006. (2006), "Code for acceptance of wind turbines generator systems", *Beijing: Chinese machinery industry press*.
- GB50009-2012. (2012), "Load code for the design of building structures", *Beijing. China building industry press*.
- Germanischer Lloyd. (2010), Guideline for the certification of wind turbines, *Hamburg: Germanischer Lloyd*.
- Han, Y., Le, C., Ding, H., Cheng, Z. and Zhang, P. (2017), "Stability and dynamic response analysis of a submerged tension leg platform for offshore wind turbines", *Ocean Eng.*, **129**, 68-82.
- Hemmatpour, M.H., Mohammadian, M. and Gharaveisi, A.A. (2016), "Simple and efficient method for steady-state voltage stability analysis of islanded microgrids with considering wind turbine generation and frequency deviation", *Iet Generation Transmission & Distribution*, **10**(7), 1691-1702.
- Jeong, M.S., Kim, S.W., Lee, I., Yoo, S.J. and Park, K.C. (2013), "The impact of yaw error on aeroelastic characteristics of a horizontal axis wind turbine blade", *Renew. Energ.*, **60**, 256-268.
- Ke, S.T., Yu, W., Wang, T.G., Ge, Y.J., Tamura, Y. (2016), "The effect of blade positions on the aerodynamic performances of wind turbine system", *Wind Struct.*, **24**(3), 205-221.
- Ke, S.T., Yu, W., Wang, T.G., Zhao, L. and Ge, Y.J. (2016), "Wind loads and load-effects of large scale wind turbine tower with different halt positions of blade", *Wind Struct.*, **23**(6), 559-575.
- Ke, S.T., Yu, W. and Wang, T.G. (2016), "Impact for blade position on aerodynamic performance of wind turbine system under stopped status", *J. Zhejiang University (Engineering Science)*, **50**(7), 1230-1238. (In Chinese)
- Laan, M.P., Sørensen, N.N., Réthoré, P.E. and Mann, J. (2015), "An improved k - ϵ model applied to a wind turbine wake in atmospheric turbulence", *Wind Energy*, **18**(5), 889-907.
- Laan, M.P., Sørensen, N.N., Réthoré, P.E. and Mann, J. (2015), "The k - ϵ -fP model applied to double wind turbine wakes using different actuator disk force methods", *Wind Energy*, **18**(12), 2223-2240.
- Lee, H.G., Kang, M.G. and Park, J. (2015), "Fatigue failure of a composite wind turbine blade at its root end", *Compos. Struct.*, **133**, 878-885.
- Li, B., Wen, H.T. and Gong, Z.Y. (2017), "The wind turbine tiwer rum wind-induced response analysis and

- wind vibration control research”, *Eng. Mech.* (In Chinese)
- Li, Q., Maeda, T., Kamada, Y., *et al.* (2016), “Wind tunnel and numerical study of a straight-bladed vertical axis wind turbine in three-dimensional analysis (Part I: For predicting aerodynamic loads and performance)”, *Energy*, **106**, 443-452.
- Madsen, S., Andersen, L.V. and Ibsen, L.B. (2013), “Numerical buckling analysis of large suction caissons for wind turbines on deep water”, *Eng. Struct.*, **57**(4), 443-452.
- Mawer, B. and Kalumba, D. (2016), “Stability of wind turbine foundations - accounting for gapping and eccentric loading”, *J. South African Institution of Civil Engineering*.
- Plaza, J., Abasolo, M., Coria, I., *et al.* (2015), “A new finite element approach for the analysis of slewing bearings in wind turbine generators using superelement techniques”, *Meccanica*, **50**(6), 1623-1633.
- Shaltout, M. (2015), “Stability of wind turbine switching control”, *Int. J. Control*, **88**(1), 193-203.
- Shilin, Z., Deyuan, L., Xiaohua, H., *et al.* (2010), “Buckling analysis of wind turbine tower under eccentric loading”, *Acta Energiæ solaris sinica*, **31**(7), 901-906. (In Chinese)
- Skrzypiński, W. and Gaunaa, M. (2015), “Wind turbine blade vibration at standstill conditions—the effect of imposing lag on the aerodynamic response of an elastically mounted airfoil”, *Wind Energy*, **18**(3), 515-527.
- Sun, L., Huo, Z. and Yan, S. (2015), “Numerical Studies on the Working Mechanism and Bearing Capacity of Bucket Foundations for Offshore Wind Turbines”, *J. Coastal Res.*, **73**, 478-482.
- Tempel, J.V.D. (2006), “Design of support structures for offshore wind turbines”, *Netherlands: Delft University of Technology*.
- Wang, H. and Cheng, X. (2015), “Undrained bearing capacity of suction caissons for offshore wind turbine foundations by numerical limit analysis”, *Mar. Georesour. Geotech.*, **34**(3), 150429065242005.

